Journal of Materials Chemistry B

ROYAL SOCIETY OF CHEMISTRY

PAPER

View Article Online
View Journal | View Issue

Cite this: J. Mater. Chem. B, 2024, 12, 8153

Trimetallic nanocomposites developed for efficient *in vivo* bimodal imaging *via* fluorescence and magnetic resonance†

Veronika Svačinová,[a] Aminadav Halili,[b] Radek Ostruszka,[a] Tomáš Pluháček,[c] Klára Jiráková,[bd] Daniel Jirák[be] and Karolína Šišková[*a]

Despite several attempts, *in vivo* bimodal imaging still represents a challenge. Generally, it is accepted that dual-modality in imaging can improve sensitivity and spatial resolution, namely, when exploiting fluorescence (FI) and magnetic resonance imaging (MRI), respectively. Here, a newly developed combination of (i) protein-protected luminescent Au–Ag nanoclusters (LGSN) manifesting themselves by fluorescent emission at 705 nm and (ii) superparamagnetic iron oxide nanoparticles (SPION) embedded within the same protein and creating contrast in MR images, has been investigated in phantoms and applied for *in vivo* bimodal imaging of a mouse as a proof of principle. Unique LGSN–SPION nanocomposites were synthesized in a specific sequential one-pot green preparation procedure and characterized thoroughly using many physicochemical experimental techniques. The influence of LGSN–SPION samples on the viability of healthy cells (RPE-1) was tested using a calcein assay. Despite the presence of Ag (0.12 mg mL^{-1}), high content of Au (above 0.75 mg mL^{-1}), and moderate concentrations of Fe (0.24 mg mL^{-1}), LGSN–SPION samples (containing approx. 15 mg mL^{-1} of albumin) were revealed as biocompatible (cell viability above 80%). Simultaneously, these concentration values of all components in the LGSN–SPION nanocomposite were used for achieving both MRI and fluorescence signals in phantoms as well as in a living mouse with sufficiently high resolution. Thus, the LGSN–SPION samples can serve as new efficient bimodal FI and MRI probes for *in vivo* imaging.

Received 28th March 2024,
Accepted 12th July 2024

DOI: 10.1039/d4tb00655k

rsc.li/materials-b

Introduction

Common imaging modalities used in clinical and preclinical medicine like magnetic resonance imaging (MRI), computed tomography (CT), ultrasound, single photon emission computed tomography (SPECT), positron emission tomography (PET), and optical imaging used as a stand-alone system can provide mixed results due to the individual limitations of each technique, such as low sensitivity, low spatial resolution, signal attenuation, ionizing radiation toxicity of contrast agents, and/or inaccuracy, respectively. Bi-/multi-modal imaging systems bearing the advantages of specific individual imaging modalities may overcome the limitations associated with the stand-alone systems.[1] For instance, ^{1}H MRI provides exceptional soft tissue contrast, penetration depth, and high spatial resolution, whereas fluorescence imaging (FI) manifests itself with extremely high sensitivity.[1] Therefore, the combination of dual-imaging modality exploiting ^{1}H MRI and FI, both non-ionizing methods, can lead to a great improvement in cell imaging, not only *in vitro*, but also *in vivo*. There is thus no wonder that the development of new bimodal probes for simultaneous FI and MRI represents a hot topic of current trends in diagnosis and medical imaging.

There have been several trials to prepare bimodal imaging FI and MRI probes already, as can be found in scientific literature.[2–16] Researchers have adopted four different approaches so far: (i) fluorescent species combined with magnetic complexes;[3,4] (ii) fluorescent species and magnetic nanostructures;[7,9] (iii) luminescent nanostructures and magnetic complexes;[6,8] and/or (iv) luminescent and magnetic nanostructures.[2,5,10–13,17] Nanostructures usually comprise of an inorganic core stabilized by an organic layer[18] and/or they are formed in a matrix.[19] Based on this, coupling luminescent and

[a] Department of Experimental Physics, Faculty of Science, Palacký University Olomouc, tř. 17. Listopadu 12, 77900 Olomouc, Czech Republic. E-mail: karolina.siskova@upol.cz
[b] Institute for Clinical and Experimental Medicine, Videnska 9, 140 21 Prague, Czech Republic
[c] Department of Analytical Chemistry, Faculty of Science, Palacký University Olomouc, tř. 17. Listopadu 12, 77900 Olomouc, Czech Republic
[d] Department of Histology and Embryology, The Third Faculty of Medicine, Charles University, Ruská 87, 100 00 Prague, Czech Republic
[e] Faculty of Health Studies, Technical University of Liberec, Studentska 1402/2, 46117 Liberec, Czech Republic

† Electronic supplementary information (ESI) available. See DOI: https://doi.org/10.1039/d4tb00655k

magnetic nanostructures is very promising because nanostructures can be designed with desired sizes and shapes by appropriate tuning of synthetic parameters. Moreover, nanostructure surfaces can be functionalized with organic species either during and/or after their formation quite easily, thus leading to stabilization of their unique physicochemical properties, stemming from inorganic parts mostly. In other words, stabilized nanostructures are less prone to changes in their important characteristics induced by the surrounding environment compared with molecular species (*e.g.*, regular fluorescent dyes) and/or complexes (*e.g.*, Gd-based).

Current MRI contrast agents, primarily Gd-based, come with inherent risks of systemic and organ-specific toxicity, leading to safety concerns. Consequently, there is a growing interest in exploring alternative contrast agents for ^{1}H MR imaging, based on superparamagnetic iron oxide nanoparticles (SPION)[20] or non-hydrogen MR (referred to as X-nuclei MR)[21–24] contrast agents being the most common alternatives. Among these, SPION-based contrast agents have gained widespread use due to unique superparamagnetic properties. Moreover, SPION are widely recognized as inert imaging agents devoid of intended pharmacological functions.[25] These nanoparticles are commonly classified as biocompatible, demonstrating negligible *in vivo* toxicity.[26,27] Several variations of SPION, coated with a range of bio-molecular species, have already received approval from the federal drug administration (FDA).[28] They show promise as potential candidates due to their efficient biodegradability, as demonstrated by Ehlerding.[29]

Among various luminescent nanostructures, protein-/peptide-stabilized gold and/or gold–silver nanoclusters are suitable for FI due to their unique optical properties such as: tunable emission reaching the near infrared (NIR) region, high photostability, long luminescence lifetimes (units of microseconds), large Stokes shifts (above 100 nm), functionality, easy bioconjugation, and excellent biocompatibility.[28–33] Already in 2010, protein-stabilized-AuNCs (gold nanoclusters) were used as novel contrast FI agents for *in vivo* imaging.[34] Since then, a bimodal imaging platform (however, FI + CT) based on luminescent gold nanoclusters and their further intrinsic property has been exploited.[35] Very recently we have reported a successful combination of AuNCs with SPION and application of this kind of bimetallic nanocomposite as an efficient bimodal imaging probe in mice.[19] Nevertheless, no report about *in vivo* imaging exploiting the combination of luminescent protein-templated Au–Ag nanoclusters (LGSN) and SPION has been published so far, to the best of our knowledge. The unique combination of functional LGSN and SPION nanostructures, embedded in the most abundant blood protein in mammals (serum albumin) and representing a new bimodal FI and MRI contrast agent, is thus the first of its kind.

Since we considered the importance of protein corona formation around nanocomposites under *in vivo* conditions,[36] we have chosen albumin as a protein template and reducing agent simultaneously. It is well-known that albumin participates in the regulation of plasma colloid osmotic pressure and transports endogenous and exogenous ligands, making albumin a useful protein for biomedical applications.[37] Our synthetic procedure of LGSN–SPION samples is made as simple as possible, reproducible, and obeys principles of a green chemistry approach to nanocomposite formation. Indeed, LGSN–SPION nanocomposites (denoted also as trimetallic nanocomposites in the present work) were prepared on the basis of the optimized preparation procedure of bimetallic (AuNCs and SPION) nanocomposites published by us very recently.[19] In the present study, a third metal (Ag) was added to improve the optical properties of the dual-responsive nanocomposites (as demonstrated in this work), and for potential antibacterial effect and/or future theranostic application. Moreover, since the newly developed LGSN–SPION nanocomposites provided suitable characteristic MR and fluorescence properties for bimodal FI and MR imaging in phantoms, their applicability as a new bimodal FI and MRI inert contrast agent was tested in living mice and proven to be successful.

Results and discussion

Unique green synthesis of LGSN–SPION nanocomposite

Our synthetic approach (schematically depicted in Fig. 1) is dissimilar to any preparation procedures employed by authors

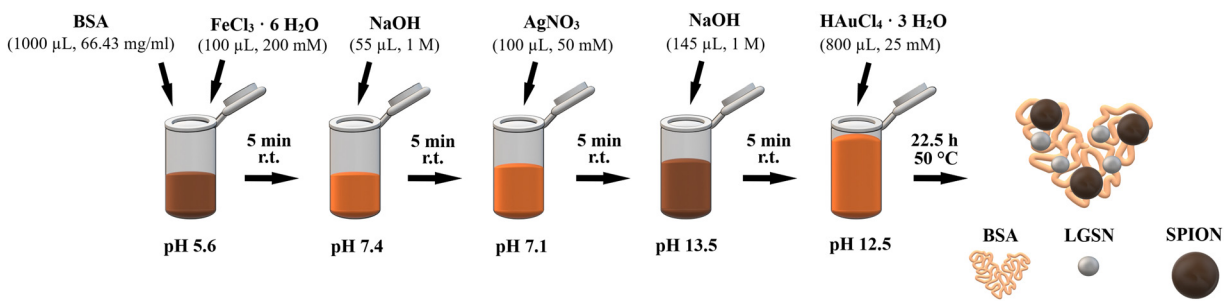

Fig. 1 Schematic depiction of LGSN–SPION synthesis: the volumes and concentrations of the used aqueous solutions of particular reactants are specified, the pH value in each step of the synthesis is given as well. The time between additions of reactants solutions was set to 5 minutes and almost all steps of the synthesis (with the only exception of sample maturing) were performed at room temperature. Then, the as-synthesized sample was allowed to develop (to mature) for 22.5 h at 50 °C. Subsequently, dialysis was performed to obtain the final trimetallic nanocomposite (*i.e.*, LGSN–SPION nanocomposite) that was characterized and tested as a new bimodal contrast agent.

who used bovine serum albumin (BSA) and/or glutathione as templating and reducing agents and introduced Au(III) and Ag(I) ions to prepare bimetallic AuAg nanoclusters with improved optical properties.[14,38,39]

In our experiments (Fig. 1), delicate adjustments of the pH value during the synthetic procedure, way of mixing reactants, order of reactant addition, time of particular reaction, temperature of reaction mixture, *etc.* need to be carefully optimized at the same moment to increase the content of metals within the final LGSN–SPION nanocomposites and to avoid any precipitate formation. Indeed, the researchers used either a co-precipitation technique,[14] or anti-/galvanic exchanges.[38,39] In several cases, the formation of AgCl precipitate was observed,[14,38] which decreased the final content of Ag unpredictably.

To obtain stable trimetallic nanocomposites in a reproducible way, we allowed ferric ions to interact with the protein (BSA) for a certain period. Subsequent adjustment of the pH value back to approximately 7.4 resulted in the formation of a neutral charge of iron aqua complex in the solution, thereby facilitating the binding of ferric ions to the albumin molecules.[40] Afterwards, silver Ag(I) and then gold Au(III) ions were reacted with BSA–Fe(III) complexes under strongly alkaline conditions. As demonstrated in our previous work, iron cations bind preferentially to oxygen-terminated functional groups of amino acid residues within BSA, while gold preferentially binds to sulphur-terminated ones.[41] The binding preferences of silver cations are very similar to those of gold cations, *i.e.*, toward sulphur as is generally known. It can thus be envisaged that the protein-bound iron cations will not interfere with, nor hinder the incorporation of noble metal cations into the protein structure. Due to the addition of Ag(I) prior to Au(III) that is followed by immediate alkalization, we assume that Ag nanoclusters may be formed first, enabling then the galvanic exchange in the next step when gold cations are introduced. Subsequent prolonged heating of the reaction mixture resulted in an increased rate of SPION and LGSN formation. The optimal theoretical molar ratio of BSA : Au : Ag : Fe was determined to be 1 : 20 : 5 : 20 and was based on our previous[19] optimized bimetallic (AuNCs–SPION) systems where the theoretical molar ratio of BSA : Au : Fe was set to 1 : 20 : 20. The Ag(I) addition is intentional and should improve the fluorescent features of the final unique trimetallic nanocomposites.

LGSN–SPION main characteristics with respect to their bio-application

Efficiency of metals incorporation within a trimetallic nanocomposite and HR-TEM/STEM visualization. The accurate concentrations of each metal content within the as-synthesized LGSN–SPION nanocomposites were determined using ICP-MS (inductively coupled plasma mass spectrometry). All experimental and theoretical values of particular metal concentrations are listed in mg mL^{-1} in Table 1 (while in mM in Table SI-1 in the ESI;† further details about the ICP-MS method are given in Tables SI-2–SI-4, ESI†).

From the ratio of experimental/theoretical concentrations, it is clear that the efficiency of particular metal incorporation within the trimetallic nanocomposites is the highest for Ag (around 99%), followed by that of Fe (around 94%), and the lowest is obtained for Au (around 84%). The lowest efficiency of Au incorporation may be caused by its addition in the final steps of the synthetic procedure (Fig. 1), when potential binding sites for metals within the denatured protein structure may be occupied by Fe and/or Ag already.

The structure of LGSN–SPION nanocomposites was investigated using HR-TEM, applying HAADF mode; a randomly chosen place is shown in Fig. 2(A). Elemental mapping using EDS was performed for the same place and revealed a high content of Fe, Au, Ag, S, O, C, N (all stemming from the sample), and Cu (coming from the TEM grid) as clearly seen in Fig. 2.

Obviously, Au, Ag, and S (similarly N and C, but they are not shown: the former for redundancy, and the latter for parasitic coincidence with the carbon layer stemming from the substrate) are homogeneously spread on the TEM-grid. In contrast, iron with oxygen can be co-localized frequently in the form of agglomerates. This corresponds with the reactivity and binding preferences of each metal (noble metals *vs.* a common metal). Furthermore, the presence of iron(III) oxide has been unequivocally confirmed using Mössbauer spectroscopy (Fig. SI-1 in the ESI†).

Size and charge of the LGSN–SPION nanocomposite. The hydrodynamic diameter and zeta potential of nanocomposites are among the crucial factors used for predictions in their behavior within living organisms.[28] Therefore, we determined the average hydrodynamic diameter and zeta potential values using DLS. The *Z*-average value of the LGSN–SPION nanocomposite

Table 1 Theoretical and experimental (determined using ICP-MS for samples in triplicate) values of component concentrations (expressed in mg mL^{-1}) in LGSN–SPION nanocomposites after dialysis; the average experimental values are listed as well

Protein	Au			Ag			Fe		
c(th) [mg mL^{-1}]	*c*(th) [mg mL^{-1}]	*c*(exp) [mg mL^{-1}]	*c*(exp)/*c*(th)	*c*(th) [mg mL^{-1}]	*c*(exp) [mg mL^{-1}]	*c*(exp)/*c*(th)	*c*(th) [mg mL^{-1}]	*c*(exp) [mg mL^{-1}]	*c*(exp)/*c*(th)
20.13	1.20	1.01	0.84	0.16	0.16	1.00	0.34	0.32	0.94
		1.02	0.85		0.16	0.99		0.32	0.94
		1.00	0.83		0.16	0.99		0.32	0.94
Average value	n.a.	1.01	0.84	n.a.	0.16	0.99	n.a.	0.32	0.94

Note: *c*(th) means theoretical concentration; *c*(exp) means experimentally determined concentration; n.a. means not applicable.

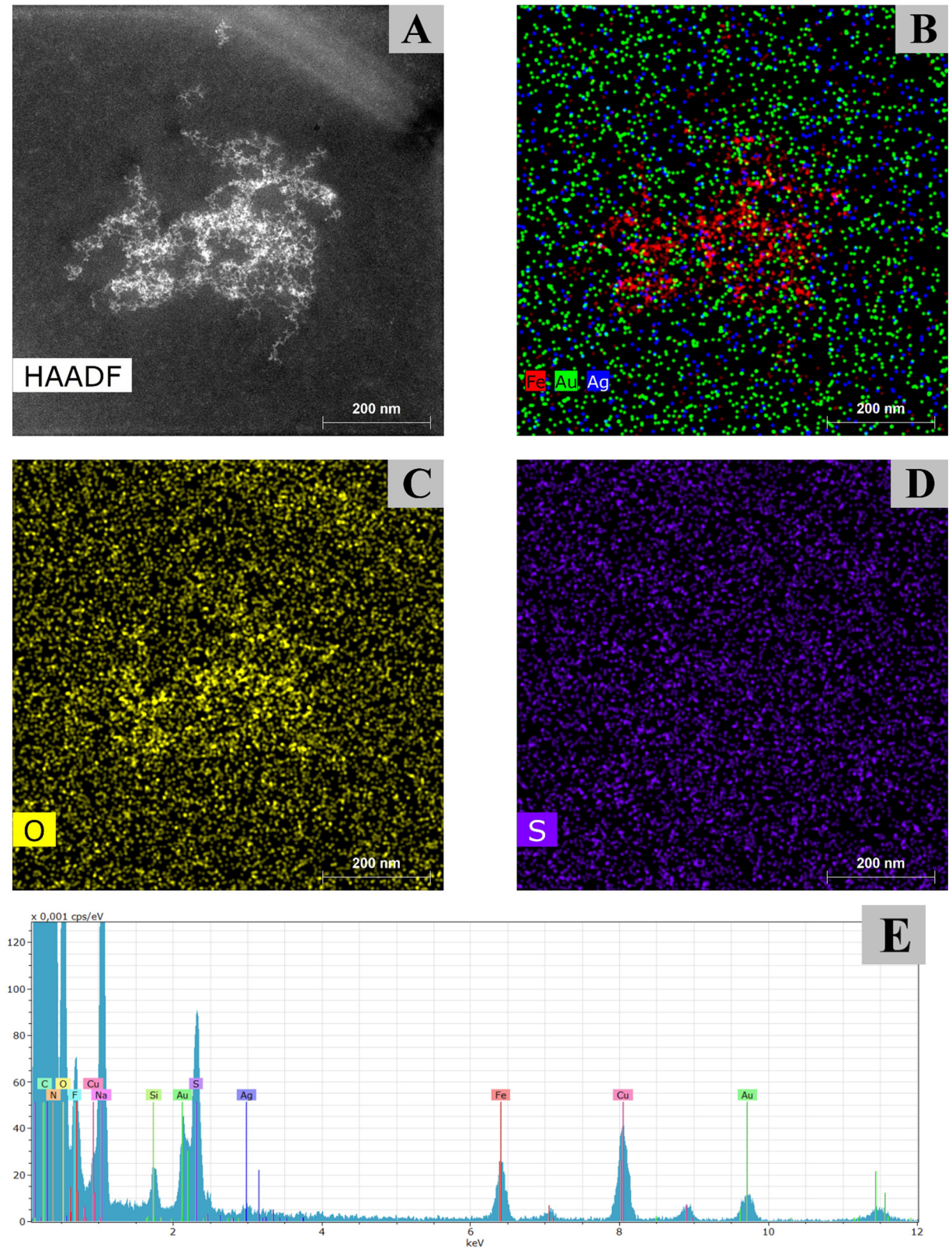

Fig. 2 HR-TEM image of a representative LGSN–SPION sample (A), and elemental mapping made by EDS (energy dispersive spectroscopy) for the determination of chosen elements distribution within a particular area: metals like gold, silver, and iron are highlighted in (B), while oxygen is shown in (C), and sulphur in (D); all belonging to the LGSN–SPION composite. The whole EDS spectrum is shown in (E) and provides information about elemental composition in the area that was mapped and is shown in (A). Note: Cu stems from the microscopic grid serving as a substrate for the sample, whereas Na, Si, and F may come from impurities distributed within the LGSN–SPION sample.

reached 214.5 ± 3.4 nm and a negative zeta potential of −43.8 ± 2.0 mV was recorded frequently (Table SI-5, ESI†).

The *Z*-average value of our newly developed LGSN–SPION nanocomposite is comparable with that of bimetallic AuNCs–SPION embedded in the same protein;[19] the zeta potential value of our LGSN–SPION nanocomposite resembles that obtained by Shankar *et al.* for monometallic AuNCs.[42] A certain type of monometallic BSA–SPION nanocomposites exhibited lower *Z*-average and zeta potential values.[43,44] We can thus sum up that the size and charge of our newly developed trimetallic nanocomposite fall within the range of hydrodynamic diameters (hundreds of nm) and zeta potential values (negative) observed by other authors for particular monometallic and/or bimetallic systems.

The particle size distribution based on intensity changes of the scattered light (measured by DLS) is plotted in Fig. SI-2 (ESI†). It is obvious that only one peak is present in the graph of LGSN–SPION nanocomposite (Fig. SI-2, ESI†), whereas three peaks were observed in our bimetallic AuNCs–SPION nanocomposites.[41] This corresponds to the improved polydispersity index (PDI) value of the newly developed trimetallic nanocomposites, reaching the value of 0.31 ± 0.03 (Table SI-5, ESI†), *i.e.*, a less broad size distribution in LGSN–SPION than in the bimetallic case, where PDI equals 1.0.[41] We attribute the improved PDI of LGSN–SPION nanocomposites to the changes made in the synthetic approach.

Luminescence of the LGSN–SPION nanocomposite. LGSN–SPION nanocomposites with the emission maximum positioned at 705 nm (using 440 nm excitation), Fig. 3, can be considered as more suitable for *in vivo* fluorescence imaging than bimetallic AuNCs–SPION analogues.[19,38] The excitation wavelength was chosen from the measured excitation–emission luminescence 3D map (Fig. SI-3, ESI†). It can be clearly seen from Fig. SI-3 (ESI†) that the higher wavelength of excitation used (within the visible region) leads to the lower luminescence intensity. Therefore, the excitation wavelength within the visible region was chosen for the subsequent *in vitro* as well as *in vivo* measurements. In contrast to monometallic luminescent AuNCs entrapped in BSA, which are characterised by their luminescence at around 655 nm,[45,46] the presence of silver ions within the luminescent nanocomposite may cause a red-shift of the emission maximum.[14,38,39] In addition, AgNCs may exhibit red luminescence with a maximum at 685 nm.[47] The position of the fluorescence emission maxima of a luminescent species is a tremendously important factor for its potential *in vivo* application as a FI probe because one of the biological optical windows begins at around 650 nm (so called near infrared region I). The emission of AuNCs is located close to the edge of this window and, hence, might not be very suitable for *in vivo* bio-imaging.

In Fig. 3, the emission bands of our newly developed LGSN–SPION nanocomposite and bimetallic AuNCs–SPION (representing a reference) are compared directly. Besides different positions of emission maxima, the full width at half maximum (FWHM) for the LGSN–SPION nanocomposite equals 180 nm, while that of AuNCs–SPION is 150 nm (Fig. 3). A wider FWHM may suggest a somewhat broader size distribution of the luminescent part of our newly developed LGSN–SPION nanocomposites, *i.e.*, varying sizes of luminescent LGSN differing by a few noble metal atoms.

The broader size distribution of luminescent nanostructures within LGSN–SPION samples as compared to bimetallic nanocomposites (derived from luminescence measurements and shown in Fig. 3) is in direct contrast to the improved PDI values of LGSN–SPION (discussed in the previous section). However, the hydrodynamic diameter determined by DLS reports the average size of the whole trimetallic nanocomposite, whereas sizes of only luminescent entities are reflected in fluorescence spectra. Moreover, the differences in FWHM and/or PDI when comparing trimetallic and bimetallic nanocomposites, can both be related to the changes made in the synthetic procedure (*i.e.*, the inclusion of an additional step of Ag(I) introduction).

Furthermore, it should be noted that we tried to determine the fluorescence quantum yield (FQY) of LGSN–SPION. However, due to the strong absorption of SPION at the used fluorescence excitation wavelength (440 nm), the accurate determination of FQY is limited. Therefore, we tried to prepare SPION-free samples under identical experimental conditions (as those used in the LGSN–SPION case). The position of emission maximum and FWHM value were considered as the main criteria of similarity between LGSN–SPION and SPION-free samples. Then, the highest similarity was obtained for the sample denoted as HCl–AuAgBSA-850 mM–NaOH (description provided in Section Experimental, Synthesis, dialysis, and concentrate formation and fluorescence characteristics in Fig. SI-4 and Table SI-6 in the ESI†). The FQY value of the SPION-free sample reached almost 6% (Table SI-6, ESI†), which is

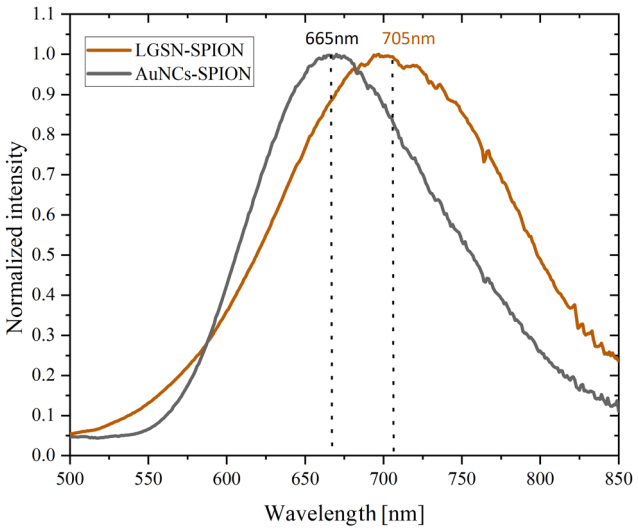

Fig. 3 Normalized fluorescence emission spectra of LGSN–SPION, trimetallic nanocomposite newly developed within this work (red curve), and AuNCs–SPION, a bimetallic nanocomposite serving as a reference (black curve); the excitation wavelength of 440 nm was applied in both cases for the sake of a direct comparison of their emission characteristics. Emission maxima are marked at 665 nm and at 705 nm for the bimetallic and trimetallic nanocomposites, respectively.

comparable with the value obtained for monometallic nanocomposite in one of our previous works.[45,46]

To determine the photostability of LGSN–SPION, we simulated conditions during an *in vivo* experiment: the fluorescence emission was measured in the cultivation medium and/or PBS, and the integral intensity of fluorescence emission and position of emission maximum were monitored over time at 37 °C. These values were related to the values obtained when the fluorescence of LGSN–SPION in deionized water was measured as a function of time at 37 °C (Fig. SI-5 and SI-6, ESI†). The very good photostability of LGSN–SPION was revealed. Considering the fact that the luminescent properties of the nanocomposites are very sensitive to any changes in the closest environment of the luminescent nanoclusters as we know from our previous work,[19] as well as from many studies of other authors, the revealed photostability in the cultivation medium represents a very important proof of our nanocomposites' stability and their suitability for further experiments, namely for those performed *in vivo*. It should be noted that the cultivation medium manifests itself by a fluorescence emission positioned close to the emission of LGNS-SPION (Fig. SI-7, ESI†). Therefore, a deconvolution of the measured fluorescence signal of LGSN–SPION in the cultivation medium into two peaks has to be done (Fig. SI-8, ESI†) prior to the fluorescence integral intensity calculation.

Cell viability tests (AM calcein assay). The biocompatibility of the newly developed LGSN–SPION nanocomposite is crucial when considering its use as a dual imaging probe in living organisms. The trimetallic nanocomposites were synthesized following green chemistry principles, thus presuming their potential non-toxicity. Both SPION and AuNCs have been extensively studied for cytotoxicity, and they are generally considered biocompatible. Several studies have demonstrated the biodegradability of SPIONs,[29] and AuNCs manifested a reasonable rate of renal clearance (*e.g.*, ref. 48). However, it is worth noting that the introduction of Ag(I) ions, in the form of silver nitrate, during the synthesis, raises concerns regarding potential toxicity. Although it is likely that Ag(I) ions are covalently bound to protein molecules, rendering them potentially non-toxic, silver nanostructures in general have been associated with cytotoxicity due to the release of Ag^+ ions. Therefore, cytotoxicity has to be determined for the LGSN–SPION nanocomposite.

For cell viability testing, an AM calcein assay was used by us although an Alamar blue assay (resazurin as a dye) and MTT assay have frequently been used in many studies for determining cell viability.[49,50] We pinpoint that methods like Alamar blue and MTT are based on a dye reduction by living cells. Unfortunately, BSA, contained in the trimetallic nanocomposites, has the ability to reduce the dyes, leading thus to the nanocomposite cytotoxicity under- or overestimation, respectively.[51] Conversely, AM calcein assay is based on a different principle than reduction. AM calcein with a bound acetal group through an ester bond becomes fluorescent after cleaving the ester bond by the living cell.

In the present study, cytotoxicity was determined using RPE-1 cells (healthy cell line) and concentrated and/or diluted forms of LGSN–SPION samples. Cell viability was evaluated to exceed 80% for the highest concentration of LGSN–SPION nanocomposites (0.12 mg mL^{-1} Ag, 0.75 mg mL^{-1} Au, 0.24 mg mL^{-1} Fe, approx. 15 mg mL^{-1} albumin), see Fig. SI-9 in the ESI,† meaning nontoxic species according to ISO 10993. Here, it should be stressed that the highest nanocomposite concentration tested in our cell viability assay, corresponded to the sample concentration used during *in vivo* imaging (presented in the next sections). The diluted LGSN–SPION nanocomposites were also tested and proved LGSN–SPION as a non-toxic species (Fig. SI-9 in the ESI†). Therefore, the tests of cell viability evidenced that the newly developed LGSN–SPION nanocomposite is biocompatible despite the presence of silver. This may be caused by sufficiently strong bonding of silver within the trimetallic nanocomposite that is achieved using a specific sequential one-pot green synthetic preparation of LGSN–SPION.

It can be stated that there are also studies involving bimetallic Au–Ag nanostructures,[52] where electron transfer between Au and Ag occurs, leading to a reduced Ag^+ release and, consequently, lower toxicity compared to stand-alone silver nanostructures. Therefore, the obtained biocompatibility of LGSN–SPION samples coincides with biocompatibility data of other researchers.

Bio-application of LGSN–SPION

Optical imaging using a trimetallic nanocomposite in phantoms. Despite knowing the optimal fluorescence excitation and emission maxima of LGSN–SPION nanocomposites (440 nm and 705 nm, respectively) derived from measurements performed in quartz cuvettes and using a regular laboratory steady-state spectrofluorometer, it was necessary to verify these values on another machine that is designed for *in vivo* fluorescence imaging. Thus, the fluorescence of LGSN–SPION samples was examined in four different concentrations introduced into glass tubes (phantoms) (Fig. 4).

The best signal of fluorescence in phantoms was achieved at an excitation wavelength of 430 nm and emission wavelength of 730 nm (*i.e.*, slightly shifted with respect to the ex/em maxima obtained using a steady-state fluorescence spectrometer; differences can be caused by variations in experimental arrangements of the instruments). The highest emission signal came from 75% nanocomposite concentration, and the lowest from 25% sample concentration. The lower signal of 100% than that of 75% nanocomposite concentration was most probably caused by an internal filter effect. The exact values of total emission (photons per second) are listed in Table SI-7 (ESI†); the distilled water signal was subtracted as a blank. Based on the phantom measurements, the 75% concentration of the trimetallic nanocomposites was used for *in vivo* experiments.

We conducted an *in vivo* experiment by administering LGSN–SPION nanocomposites *via* subcutaneous injection into a mouse, as shown in Fig. 5.

The subcutaneous injection was intentional and aimed to assess the suitability of the nanocomposites for optical imaging, following a similar approach as described in ref. 53. The excitation and emission wavelengths were used the same as in

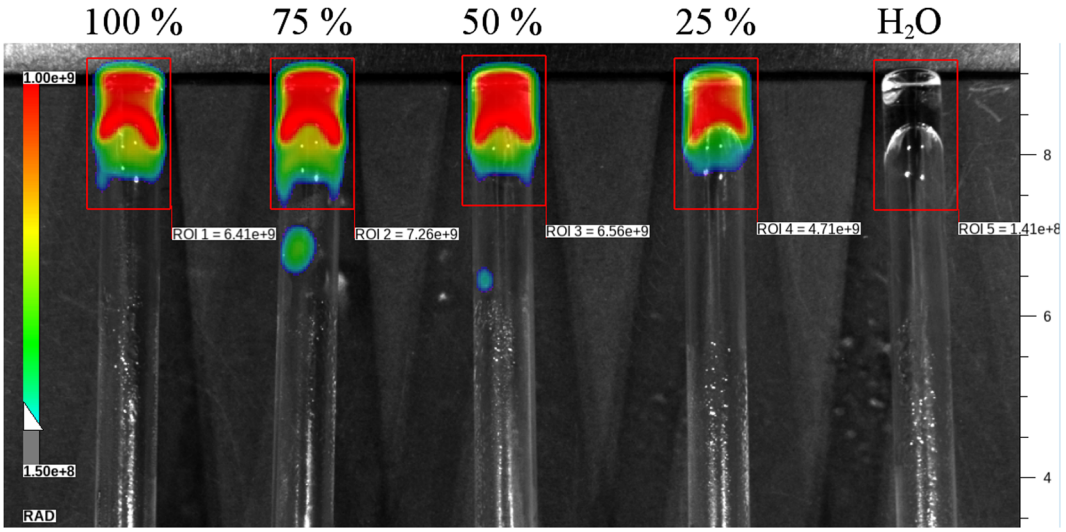

Fig. 4 Fluorescence imaging using phantoms (*i.e., in vitro* optical imaging): the excitation wavelength was set to 430 nm and the luminescence emission was recorded at 730 nm. Concentrations of protein and three selected metals within the LGSN–SPION sample denoted as 100% concentration are listed in Table 1 – briefly: the protein theoretical concentration is 20.13 mg mL^{-1}, average Au concentration (experimentally determined by ICP-MS) is 1.01 mg mL^{-1}, average Ag concentration (experimentally determined by ICP-MS) is 0.16 mg mL^{-1}, and average Fe concentration (experimentally determined by ICP-MS) is 0.32 mg mL^{-1}. The other measured samples (labeled as 75%, 50%, and 25%) are obtained by dilution of the 100% sample with deionized water.

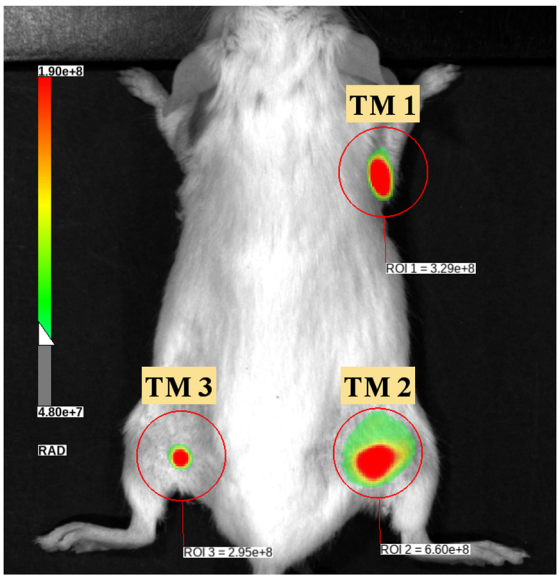

Fig. 5 Optical imaging exploiting LGSN–SPION nanocomposites in a living mouse: optimal excitation at 430 nm and emission at 730 nm. The mouse was put under complete anaesthesia and its limbs were shaved before luminescence (and subsequent MR) imaging. Thereafter, three identical samples (denoted as TM 1, TM 2, TM 3) were injected at a 75% concentration (75% of values listed in Table 1) into mouse limbs (right upper: TM 1, right lower: TM 2, and left lower: TM 3); in the fourth limb (left upper) distilled water was injected as a reference. The reference revealed no fluorescence signal under the given excitation/emission conditions.

phantom experiments (ex 430 nm, em 730 nm), shown in Fig. 4. *In vivo* imaging was also performed for a different excitation wavelength (Fig. SI-10, ESI†). Importantly, the luminescence signal of our injected trimetallic nanocomposites is sufficiently visible in all three limbs of the mouse; while no luminescent signal is observed in the limb where distilled water was injected (Fig. 5). Slight variations in the fluorescent signal intensity observed in individual limbs containing trimetallic nanocomposites (Fig. 5) can be caused by several factors: (i) position of each limb with respect to the detector was not the same; (ii) there may be differences in anatomical structures in the injection site.

So far, successful experiments of *in vivo* monitoring using solely optical probes based on monometallic and/or bimetallic luminescent nanoclusters have been made possible.[34,54–56] In the current study, our objective is to improve the *in vivo* optical imaging (*via* LGSN) by the addition of another imaging modality, such as MRI (through the incorporation of SPION in our trimetallic nanocomposites). While MRI is recognized for its superior spatial resolution, it is worth noting that it exhibits limited sensitivity compared to optical imaging. The LGSN–SPION nanocomposite is thus envisaged to be a superior contrast agent in comparison to those previously published.

MR relaxometry and imaging using the LGSN–SPION nanocomposite. SPIONs, making up the magnetically susceptible part of the trimetallic nanocomposites, serve as negative T_2 MRI contrast agents frequently.[57] The relaxation rates R_2 and R_1 were determined for four different concentrations (100%, 75%, 50%, and 25%) of the trimetallic nanocomposites in the present study. These R_2 and R_1 values were plotted in a graph as a function of the exact iron concentration (determined experimentally using ICP-MS) and were fitted with a linear function (see Fig. SI-11, SI-12 and Table SI-8, ESI†). The average relaxivities r_2 and r_1 of the LGSN–SPION nanocomposite were found to be of 2.12 ± 0.05 L mmol s^{-1} and 0.20 ± 0.01 L mmol s^{-1} values, respectively. These values are

Table 2 T_2-weighted MR images of phantoms acquired for four different concentrations of a representative LGSN–SPION sample; corresponding signal-to-noise-ratio (SNR) and contrast-to-noise-ratio (CNR) are listed

TM 1		100%	75%	50%	25%	H_2O
T_2-weighted						
	SNR	7.63	10.28	12.63	14.14	16.16
	CNR	8.52	5.88	3.53	2.02	—

comparable to the r_2 and r_1 value obtained for the bimetallic AuNCs–SPION nanocomposite.[19] The ratio r_2/r_1 is of approximately 10, which is similar to the values observed in commercial contrast agents containing SPION, such as Resovist or Feridex.[58] Relaxometry data suggest that LGSN–SPION nanocomposites can affect T_2 MR contrast but have a negligible impact on T_1 contrast. This finding is further supported by MR imaging data. In our MRI experiment, phantoms containing trimetallic nanocomposites were visualized at four different concentrations (100%, 75%, 50%, and 25%). Distilled water was used as a control, following a similar approach to optical imaging. The phantoms of a representative sample are detailed in Table 2 (T_2-weighted). T_1-weighted MR phantoms images of the representative sample are then shown in Table SI-9 (ESI†).

It is evident that the T_2 contrast between a particular sample and the signal of water is sufficiently high to be detected at all four concentrations of the newly developed LGSN–SPION nanocomposites (Table 2). This observation is further supported by quantitative analysis, where we calculated the contrast-to-noise ratio (CNR); even for the lowest tested concentration (25%), CNR was approximately 2. Note that in the case of the T_1 contrast, the signal from all phantom concentrations was practically the same and did not differ from that of water.

Based on the results obtained from the phantom study, *in vivo* MR imaging (Fig. 6) was performed exploiting 75% concentration of LGSN–SPION samples, administrated subcutaneously into individual limbs (right upper: TM 1, right lower: TM 2, and left lower: TM 3), with distilled water serving as a reference (left upper limb). Importantly, T_2 contrasts of the trimetallic samples are clearly distinguishable from surrounding tissue (Fig. 6).

It should be noted that the weight of the examined mouse (a female mouse) was monitored after three months counting from the end of the imaging experiment, and her weight increased by 10%. Furthermore, visual inspection of the areas on the animal's body where the contrast agent was applied did not show signs of inflammation or other pathologies. This supports the conclusion from cytotoxicity testing that the trimetallic nanocomposite has no harmful effects and can be considered biocompatible.

LGSN–SPION nanocomposite potentially relevant to preclinical research. Furthermore, it is important to mention that relaxometry was conducted at 1.5 T, a magnetic field

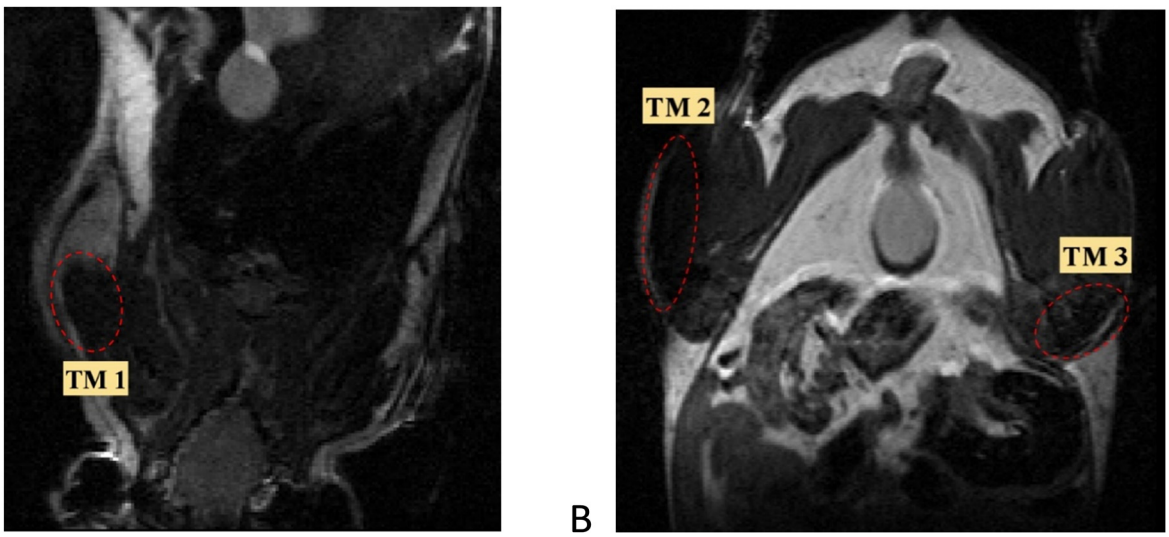

Fig. 6 MRI using a representative LGSN–SPION sample injected subcutaneously in limbs of a living mouse (upper limbs in (A), whereas lower limbs in (B)). We calculated CNR values for TM1, TM2, and TM3 as follows: CNR of TM1 = 6.69, CNR of TM2 = 6.69, and CNR of TM3 = 6.85. These values were derived from coronal T_2-weighted images, and no additional filters or post-processing adjustments were applied to the images.

strength commonly used in clinical practice. Additionally, MR imaging was performed at 4.7 T, which closely approximates the clinical field strength of 3 T. Consequently, our study results have relevance for clinical research, and our data provide valuable support for potential translation into clinical applications. Although our current study is of a proof-of-concept character, LGSN–SPION nanocomposites could be considered as inert imaging probes when their characteristics are compared with those of another inert imaging agent.[25] Moreover, further experiments in the direction of targeting are envisaged for trimetallic nanocomposites, which might be reached by their surface modification for instance.

Experimental

Chemicals

Synthesis of LGSN–SPION nanocomposites. Bovine serum albumin (BSA; >98%), gold(III) chloride trihydrate ($HAuCl_4 \cdot 3H_2O$; ≥99.9%), iron(III) chloride hexahydrate ($FeCl_3 \cdot 6H_2O$; ≥99%), silver nitrate ($AgNO_3$; 99.9999%,) and sodium hydroxide (NaOH; ≥98.0%) were purchased from Sigma-Aldrich (Saint Louis, MO, USA) and used as received (without any further purification) for all experiments. Hydrochloric acid (35%) was purchased from Penta s.r.o. (Prague, Czech Republic). Deionized (DI) water prepared by purging Milli-Q purified water (Millipore Corp., Bedford, MA, USA) was used in all experiments.

Inductively coupled plasma-mass spectroscopy (ICP-MS)

Nitric acid (69%, Analpure), hydrochloric acid (36%, Analpure), single element certified reference materials, aqueous calibration standard solution, ASTASOL® of Au, Ag, Fe (1000.0 ± 2.0 mg L^{-1}), and INT-MIX 1 (10 mg L^{-1}) were purchased from Analytika, Ltd, Prague, Czech Republic. Ultrapure 18.2 MΩ cm water was prepared using a Milli-Q purification system (Millipore Corp. Molsheim, France) and used only for ICP-MS analyses.

Cell viability

Fetal bovine serum (FBS), L-glutamine, penicillin–streptomycin and trypsin (from the porcine pancreas) were purchased from Sigma-Aldrich (Saint Louis, MO, USA). Sodium chloride (NaCl; p.a.), potassium chloride (KCl; p.a.), potassium dihydrogen phosphate (KH_2PO_4; p.a.), and disodium hydrogen phosphate (Na_2HPO_4; p.a.) were purchased from Penta chemicals (Prague, Czech Republic) and Lachem (Lanškroun, Czech Republic). Calcein AM and Dulbecco's modified Eagle's medium (DMEM, 11054, no phenol red) were purchased from Thermo Fisher Scientific (Waltham, MA, USA).

In vivo imaging

Isoflurane 5% for induction and 1.5–2% for maintenance was purchased from Baxter (Deerfield, USA) and eye cream Ophtalmo-Septonex from Zentiva (Prague, Czech Republic).

Synthesis, dialysis, and concentrate formation

The synthesis of LGSN–SPION nanocomposite was carried out in a microcentrifuge tube. To mix the sample, a vortex and pipette were used. The time period elapsed between subsequent additions of each reactant was set to 5 minutes. Firstly, $FeCl_3 \cdot 6H_2O$ (100 μL, 200 mM) was put into the microcentrifuge tube. Then, BSA solution (1000 μL, 66.43 mg mL^{-1}) was added in two steps: the first 500 μL of BSA was slowly pipetted and thoroughly mixed using the pipette; the second portion of BSA was added using the same procedure and the solution was mixed in the vortex. Subsequently, NaOH (55 μL, 1 M) was pipetted onto the wall of the microcentrifuge tube to adjust the pH to 7.4. The solution was swirled in the vortex (for approximately 30 seconds) immediately after adding NaOH. The solution was cloudy, it contained agglomerates that dissolved within a few minutes and the solution became clear. Thereafter, $AgNO_3$ (100 μL, 50 mM) was introduced into the tube and swirled. Further NaOH (145 μL, 1 M) was pipetted into the wall of the microcentrifuge tube to increase the pH above 12. The solution was instantly rigorously swirled again. Finally, $HAuCl_4 \cdot 3H_2O$ (800 μL, 25 mM) was carefully added into the solution, mixed using the pipette and swirled in the vortex. After development at 50 °C (set temperature on the dry bath incubator) for 22.5 hours, the sample changed its hue from orange to brown-orange.

HCl–AuAgBSA and HCl–AuBSA were prepared as SPION-free samples under the same conditions as LGSN–SPION, however, without $FeCl_3 \cdot 6H_2O$ and/or $AgNO_3$ (and/or both – the case of HCl–AuBSA). In fact, HCl (200 mM, 100 μl) was used instead of $FeCl_3 \cdot 6H_2O$ and diH_2O instead of $AgNO_3$. At first NaOH addition, the adequate volume was chosen so that the pH reached 7.4 (25 μl of 1 M NaOH and 30 μl of 850 mM NaOH). HCl–AuAgBSA-850 mM–NaOH was synthesized and served as a SPION-free sample manifesting itself by the same position of emission maximum as that of the LGSN–SPION nanocomposite. It is then used for fluorescence quantum yield estimation (further explanation is given in the main text below).

The samples were dialyzed with a 14 kDa cut-off dialysis membrane (regenerated cellulose, Membra-Cel TM) against deionized water. Dialysis was performed for 5 hours at room temperature (22 °C). The DI water was changed four times (time between changes: 30 min, 45 min, 60 min, 75 min; the end of the dialysis in another 90 minutes). After the dialysis, the final samples were 1.5 times diluted when compared to the volume reached immediately after the synthesis. The final trimetallic sample was used in phantoms and *in vivo* experiments. The nanocomposites were synthesized in triplicate to get statistics.

The final LGSN–SPION sample was concentrated for the purpose of cell viability testing exclusively. The concentrated sample was formed using a centrifugal concentrator (30 kDa). The relative centrifugal force was set to 3000 × *g*. Concentrate formation was performed for 5 minutes in several repetitions until the desired sample concentration was reached (*i.e.*, 2.5 times higher than the concentration reached immediately after the synthesis). After each centrifugal step, the sample was mixed using a pipette within the concentrator to destroy any

potential sediment formation at the bottom of the concentrator. Dialyzed and concentrated samples were stored at 4 °C.

ICP-MS

The modified ICP-MS method[41] was utilized to accurately determine the gold, silver, and iron concentrations in dried LGSN–SPION aliquots. The drying was realized in a vacuum rotary evaporator. Briefly, the dried aliquots were quantitatively transferred into the Teflon digestion vessels containing 2 mL of concentrated nitric acid and 2 mL of concentrated hydrochloric acid. The vessels were tightly closed with Teflon caps and the samples were digested in an MLS 1200 mega closed vessel microwave digestion unit (Milestone, Italy) according to the seven steps power controlled digestion program (ESI,† Tables S1–S3). The digests were allowed to cool down to laboratory temperature and diluted with the ultrapure water in either 25 mL or 50 mL volumetric flasks to meet the optimal working range of the ICP-MS instrument operating under the trace elemental conditions.

The total silver, gold, and iron concentrations were determined using an Agilent 7700× ICP-MS (Agilent Technologies Ltd, Japan) fitted with an octopole reaction system working in He mode to overcome the possible spectral interferences. The optimized ICP-MS conditions as well as the validation results, are summarized in the ESI.† The quality control sample at the concentration level of 500 μg L^{-1} for Ag, Fe, and 5000 μg L^{-1} for Au was analyzed every ten samples to ensure the quality of the acquired results. All ICP-MS measurements were performed in six replicates, and the results are expressed as an average ± standard deviation (SD).

HR-TEM/EDS

LGSN–SPION (the final protein concentration of 0.3 mg mL^{-1}) were drop-cast (2–4 μL) on glow discharged TEM copper grids covered with holey carbon. The drop was allowed to dry spontaneously at room temperature. Then, the samples were measured using HR-TEM Titan G2 60-300 (FEI, Hillsboro, OR, USA) with an image corrector with an accelerating voltage of 300 kV. Images were taken with a BM UltraScan CCD camera (Gatan, Pleasanton, CA, USA). Energy Dispersive Spectrometry (EDS) was performed in STEM mode using a Super-X system with four silicon drift detectors (Bruker, Billerica, MA, USA). STEM images were taken with an HAADF detector 3000 (Fishione, Export, PA, USA). The HAADF mode of STEM is intentionally used to better visualize NCs because heavier elements appear bright, while lighter elements appear dark.

Dynamic light scattering (DLS) and zeta potential measurements

The hydrodynamic diameter and zeta potential of the LGSN–SPION samples were determined using a Zetasizer Nano ZEN 3600 ZS (Malvern Instrument Ltd, Malvern, UK) equipped with a He–Ne laser. An average sample (a mix of three independently prepared samples) was measured at 22 °C.

Absorbance and fluorescence measurement

Absorbance was recorded on a Specord 250 Plus-223G1032 (Analytik Jena, Jena, Germany) with a double beam arrangement using a 1 cm quartz cuvette, 2 nm slits, data interval 1, in the range of 250–800 nm.

Fluorescence measurements of nanocomposites were taken using a JASCO F8500 (Jasco, Tokyo, Japan) spectrofluorometer in a 1 cm quartz cuvette with 2.5 nm slits, data interval of 1 nm and scan speed of 100 nm min^{-1}. Emission spectra were measured in the range of 500–850 nm using 440 nm excitation. Each sample was measured three times and subsequently the three spectra were averaged. All spectra were corrected to avoid any deviations induced by instrumental components.

The quantum yield of fluorescence (QY, F) was calculated using the following equation:

$$\phi = \phi_S \cdot \frac{F \cdot \left(1 - 10^{-A_S}\right) \cdot n^2}{F_S \cdot \left(1 - 10^{-A}\right) \cdot n_S^2}, \quad (1)$$

where F is the integrated fluorescence intensity, A is the absorbance, n is the index of refraction, and subscript s indicates the standard. DCM, 4-(dicyanomethylene)-2-methyl-6-(4-dimethylaminostyryl)-4*H*-pyran, dissolved in ethanol (99.8%, Lach-Ner, Neratovice, Czech Republic) was used as a standard (F_s = 0.437 ± 0.024).[59]

Photostability in cultivation medium and PBS

The culture medium and PBS was used for photostability determination. The LGSN–SPION was added into culture medium or PBS with a ratio of 1 : 4 (this corresponded to the dilution in cell viability testing) and it was incubated in a dry bath incubator at a set temperature of 37 °C. Integral intensity was determined over time (1 h, 2 h, 24 h 72 h and 168 h). Fluorescence measurements of LGSN–SPION in culture medium and PBS were performed on a JASCO F8500 (Jasco, Tokyo, Japan) spectrofluorometer in a 1 cm quartz cuvette with 2.5 nm slits, data interval of 1 nm and scan speed of 100 nm min^{-1}. Spectra were obtained in the range of 480–850 nm using 440 nm excitation.

Cell viability determination (calcein assay)

The cell viability was determined using the RPE-1 cell line and calcein assay. Initially, 80 μL of cultivation medium or cell suspension (5000 cells per well) was cultivated in a 96-well microtitration plate for 24 hours in an incubator (37 °C, 5% CO_2). Then, 20 μL of the DI water (first and second column) and the LGSN–SPION samples in various concentrations (the highest LGSN–SPION concentration in the cultivation medium contained: approx. 15 mg mL^{-1} albumin, 0.75 mg mL^{-1} Au, 0.12 mg mL^{-1} Ag, 0.24 mg mL^{-1} Fe) were added and incubated for 24 hours. Liquid contents of the wells were carefully removed (to eliminate its interference with calcein), and the adhered cells were rinsed using PBS twice before the addition of 100 μL of calcein. Cells were incubated with calcein in an incubator for 1 hour, and then the fluorescence was measured on a microplate reader Fluoroskan Ascent (Finland). Excitation and emission wavelengths were set at 485 nm and 538 nm,

respectively. Cell viability (C_V) was calculated using eqn (2):

$$C_V = 100 \cdot \frac{F_S - F_M}{F_C - F_M}, \quad (2)$$

where F_S is the fluorescence in the cell suspension treated with the LGSN–SPION sample, F_C is fluorescence of non-treated cells (reference), and F_M is the fluorescence of the cultivation medium (blank).

Animal preparation

Animals were housed in a temperature-controlled room with a 12-h light–dark cycle with free access to food pellets and water (responsible person: Daniel Jirák, accreditation no. CZ 02264). All animal protocols were approved by the Ethics Committee of the Institute for Clinical and Experimental Medicine and the Ministry of Health of the Czech Republic (no. 58/2014) in accordance with the European Communities Council Directive (2010/63/EU). An *in vivo* measurement was performed using healthy female BALB/c mouse as a proof of principle. The animal preparation process was carried out under the complete anaesthesia of the animal (using 5% isoflurane (Baxter, Deerfield, USA) for induction and 1.5–2% isoflurane for maintenance). To minimize optical signal attenuation, all four limbs of a mouse were carefully shaved, leaving a sufficient space around the injection site. The mouse received a subcutaneous injection of three samples (prepared using the same above-described procedure): each sample was administered into a separate limb (100 μL, 75% concentration of TM 1 into right upper limb; 100 μL, 75% concentration of TM 2 into right lower limb; 100 μL, 75% concentration of TM 3 into left lower limb). H_2O serving as a reference was injected into the fourth limb (left upper).

Optical imaging

The optical imaging was conducted using the SPECTRAL Ami HT imager, and subsequent image processing and quantification were performed using the Aura software (*via* spectral instruments imaging). The fluorescence imaging involved phantoms containing nanocomposites at four distinct concentrations: 100%, 75%, 50%, and 25%. Distilled water served as a reference. The imaging process encompassed various emission and excitation ranges to identify optimal conditions for fluorescence signal acquisition which was found at 430 nm excitation and at 730 nm emission. The other parameters were set up accordingly: excitation power = 4, exposure time = 2 s, FOV = 15, F-stop = 2, binning = 2.

Fluorescence imaging of a mouse with subcutaneously injected samples and reference was conducted immediately following the injection (100 μL of 75% nanocomposites concentration) without any delay. The animal was subjected to anaesthesia using isoflurane (1.5–2% for maintenance), and optical measurement was conducted using identical excitation/emission parameters as those applied to the phantoms.

MR imaging and relaxometry

Relaxometry measurement was used to assess the relaxation times and to calculate the relaxivities of nanocomposites dispersed in distilled water using a 1.5 T Minispec 60 MHz relaxometer (Bruker Biospin, Germany) at temperatures of 20 °C and 37 °C. Four distinct concentrations of 250 μL samples were prepared: 100%, 75%, 50%, and 25%. T_1 relaxation times were determined utilizing the inversion recovery sequence (repetition time (TR) = 0.01–10 000 ms, recycle delay = 4 s, number of acquisitions (NA) = 4, mono-exponential fitting, 10 data points per fitting). T_2 relaxation times were measured using the Carr–Purcell–Meiboom–Gill (CPMG) sequence (recycle delay = 2 s, NA = 8, echo time (TE) = 0.05 ms, mono-exponential fitting, 20 000 data points per fitting). Each sample was subjected to three measurements under identical conditions.

MR imaging was performed on a 4.7 T MR scanner equipped with a radiofrequency resonator coil (Bruker BioSpin, Germany). MR data were processed and analysed using ImageJ (version 1.46r, National Institute of Health, USA). The signal-to-noise ratio (SNR) was calculated according to equation SNR = $0.655S/\sigma$ where S is the signal intensity in the region of interest, σ is the standard deviation of background noise, and the constant 0.655 reflects the Rician distribution of background noise in a magnitude MR image. The contrast-to-noise ratio (CNR) was calculated as the difference in SNR between phantom and water (phantom study) or between an area of LGSN–SPION nanocomposite administration and the muscle.

We acquired both T_1- and T_2-weighted MR images using the Rapid Acquisition with Relaxation Enhancement (RARE) sequence. T_1: (TR = 400 ms, TE = 12 ms, NA = 8, rare factor (RF) = 1, and scan time (ST) = 10 min 14 s) spatial resolution = 137 × 137 μm^2, slice thickness = 0.6 mm. T_2: (TR = 3300 ms, TE = 36 ms, NA = 5, RF = 5, and ST = 10 min 27 s) spatial resolution = 137 × 137 μm^2, slice thickness = 0.6 mm.

In vivo measurement was performed using a healthy female BALB/c mouse as a proof of principle. The mouse was anesthetized with 5% isoflurane (Baxter, Deerfield, USA) for induction and 1.5–0.5% isoflurane for maintenance. The respiratory rate was monitored throughout the study using a trigger unit (Rapid Biomedical, Berlin, Germany). To avoid eye dryness and its potential damage, an eye cream (Ophtalmo-Septonex, Zentiva, Czech Republic) was applied before the measurement. For the animal experiment, a home-made birdcage coil was used.

Prior to MR imaging, an additional 100 μL of the samples solution and reference was injected. This additional injection was aimed at enhancing visualization and signal quality due to potential animal movement and the elapsed time between optical imaging and MRI scans, which could result in partial absorption of the contrast agent. Based on the obtained results from a phantom study, we acquired T_2-weighted MR images using the (RARE) sequence, using the following parameters: T_2: (TR = 3300 ms, TE = 36 ms, NA = 4, RF = 8, and ST = 5 min 16 s) spatial resolution = 176 × 176 μm^2, slice thickness = 0.6 mm.

Conclusions

Unique properties of multimodal probes allow scientists and doctors to use several types of bioimaging methods and, consequently, to obtain more accurate results. Each type of bioimaging technique has advantages, but also limitations. Optical imaging, namely FI, is characterized by high sensitivity, low spatial penetration, and lower resolution. On the other hand, MR imaging has good resolution, no limit for penetration, but has a lower sensitivity.[60] Therefore, more accurate *in vivo* imaging can be achieved by using a bimodal contrast agent/probe combining FI and MRI. So far, gadolinium/gold nanocomposites have been reported as an efficient bimodal FI + MRI probe for bio-imaging.[61,62] However, gadolinium ions, Gd(III), entrained in both types of multimodal probes, represent potential ecological and healthy risks.[63] In contrast, LGSN–SPION nanocomposite, newly developed by us in the present work, successfully combines two different kinds of bio-imaging, FI + MRI, while exhibiting very good biocompatibility.

The new bimodal (FI + MRI) imaging inert contrast agent made up of luminescent noble metal nanoclusters (LGSN) and superparamagnetic iron oxide nanoparticles (SPION), both embedded within the same albumin, was developed, characterized, and successfully used for *in vivo* bio-imaging. This innovative contrast agent is the first of its kind in the world: (i) suitably combining nanostructured materials leading to successful FI + MRI in a living mouse, and simultaneously, (ii) possessing the opportunity of extra functionalization. The tests of cell viability (on healthy RPE-1 cell line) evidenced that the newly developed LGSN–SPION nanocomposite is biocompatible despite the presence of silver. It may be caused by sufficiently strong bonding of silver within the trimetallic nanocomposite that is achieved by a specific sequential one-pot green synthetic preparation of LGSN–SPION samples. Further research is needed to specifically target the trimetallic nanocomposites into individual organs and/or tumor tissue. It would pave the way to potential theranostic application of modified LGSN–SPION nanocomposites.

Author contributions

VS: investigation (DLS, fluorescence), methodology (synthesis of trimetallic nanocomposite), formal analysis, original draft writing. AH: investigation (FI and MRI *in vitro* and *in vivo*). Formal analysis. RO: methodology (optimized synthesis of AuNC–SPION nanocomposite), formal analysis. TP: investigation (ICP-MS analyses), formal analysis, original draft editing. KJ: investigation (biocompatibility tests), methodology (cell viability), formal analysis, original draft editing. DJ: investigation (FI and MRI *in vitro* and *in vivo*), methodology (FI and MRI *in vitro* and *in vivo*), formal analysis, funding acquisition, original draft editing. KS: conceptualization, resources, methodology, funding acquisition, supervision, writing and editing original draft, original draft – review & editing.

Data availability

The raw/processed data required to reproduce these findings can be requested from the authors directly and sent on demand.

Conflicts of interest

There are no conflicts to declare.

Acknowledgements

Financial support by the Czech Science Foundation (project no. 19-03207S), by the Ministry of Health CR-DRO (Institute for Clinical and Experimental Medicine IKEM, IN00023001), by the Ministry of Education, Youth and Sports (Programme EXCELES, Project no. LX22NPO5104 – Funded by the European Union – Next Generation EU) and by the Internal Grant Agency of Palacký University (projects no. IGA_PrF_2024_002) is gratefully acknowledged. The authors acknowledge the assistance provided by the Research Infrastructure NanoEnviCz, supported by the Ministry of Education, Youth and Sports of the Czech Republic under project no. LM2018124. Vítězslav Heger is thanked for the verification of purity of BSA by using EDS and XRD; Jitka Prachařová is acknowledged for enabling sample drying; Petr Běčák is thanked for assisting in the early trials of LGSN–SPION preparations; Lucie Rárová is thanked for independent repetition of cell viability tests and for valuable discussions; Martin Mistrík is acknowledged for healthy RPE-1 cell line donation; Marcela Václavíková is thanked for her help with retrieval of several articles (not available *via* our institutional account).

Notes and references

1 A. S. Wadajkar, T. Kadapure, Y. Zhang, W. Cui, K. T. Nguyen and J. Yang, *Adv. Healthcare Mater.*, 2012, **1**, 450–456.
2 R. Binaymotlagh, F. Hajareh Haghighi, F. Aboutalebi, S. Z. Mirahmadi-Zare, H. Hadadzadeh and M.-H. Nasr-Esfahani, *New J. Chem.*, 2019, **43**, 238–248.
3 D. Dong, X. Jing, X. Zhang, X. Hu, Y. Wu and C. Duan, *Tetrahedron*, 2012, **68**, 306–310.
4 S. Guan, R. Liang, C. Li and M. Wei, *Talanta*, 2017, **165**, 297–303.
5 C.-L. Huang, W.-J. Hsieh, C.-W. Lin, H.-W. Yang and C.-K. Wang, *Ceram. Int.*, 2018, **44**, 12442–12450.
6 W. Le, S. Cui, X. Chen, H. Zhu, B. Chen and Z. Cui, *Nanomaterials*, 2016, **6**, 65.
7 D.-L. Li, J.-E. Tan, Y. Tian, S. Huang, P.-H. Sun, M. Wang, Y.-J. Han, H.-S. Li, H.-B. Wu, X.-M. Zhang, Y.-K. Xu and Q.-S. Wang, *Biomaterials*, 2017, **147**, 86–98.
8 G. Liang and L. Xiao, *Biomater. Sci.*, 2017, **5**, 2122–2130.
9 L. Meng, X. Ma, S. Jiang, G. Ji, W. Han, B. Xu, J. Tian and W. Tian, *J. Mater. Chem. B*, 2019, **7**, 5345–5351.
10 S. K. Pahari, S. Olszakier, I. Kahn and L. Amirav, *Chem. Mater.*, 2018, **30**, 775–780.

11 J. Sheng, X. Jiang, L. Wang, M. Yang and Y.-N. Liu, *Anal. Chem.*, 2018, **90**, 2926–2932.
12 Y. Xu, S. Palchoudhury, Y. Qin, T. Macher and Y. Bao, *Langmuir*, 2012, **28**, 8767–8772.
13 X. Su, Y. Xu, Y. Che, X. Liao and Y. Jiang, *J. Biomed. Mater. Res.*, 2015, **103**, 3956–3964.
14 J. Zhang, Y. Yuan, Y. Wang, F. Sun, G. Liang, Z. Jiang and S.-H. Yu, *Nano Res.*, 2015, **8**, 2329–2339.
15 M. Rabyk, A. Galisova, M. Jiratova, V. Patsula, L. Srbova, L. Loukotova, J. Parnica, D. Jirak, P. Stepanek and M. Hruby, *J. Mater. Chem. B*, 2018, **6**, 2584–2596.
16 O. Shapoval, H. Engstová, D. Jirák, J. Drahokoupil, K. Sulková, Z. Berková, O. Pop-Georgievski, B. Holendová, P. Ježek and D. Horák, *ACS Appl. Mater. Interfaces*, 2022, **14**, 18233–18247.
17 C. Wang, Y. Yao and Q. Song, *J. Mater. Chem. C*, 2015, **3**, 5910–5917.
18 M. F. Matus and H. Häkkinen, *Nat. Rev. Mater.*, 2023, **8**, 372–389.
19 R. Ostruszka, A. Halili, T. Pluháček, L. Rárová, D. Jirák and K. Šišková, *J. Colloid Interface Sci.*, 2024, **663**, 467–477.
20 R. Ettlinger, N. Moreno, N. Ziółkowska, A. Ullrich, H. Krug Von Nidda, D. Jirák, K. Kerl and H. Bunzen, *Part. Part. Syst. Charact.*, 2020, **37**, 2000185.
21 D. Jirak, J. Svoboda, M. Filipová, O. Pop-Georgievski and O. Sedlacek, *Chem. Commun.*, 2021, **57**, 4718–4721.
22 N. Ziółkowska, M. Vít, R. Laga and D. Jirák, *Sci. Rep.*, 2022, **12**, 2118.
23 L. Kracíková, N. Ziółkowska, L. Androvič, I. Klimánková, D. Červený, M. Vít, P. Pompach, R. Konefał, O. Janoušková, M. Hrubý, D. Jirák and R. Laga, *Macromol. Biosci.*, 2022, **22**, 2100523.
24 V. M. Panakkal, D. Havlicek, E. Pavlova, M. Filipová, S. Bener, D. Jirak and O. Sedlacek, *Biomacromolecules*, 2022, **23**, 4814–4824.
25 M. Mahmoudi, S. Sant, B. Wang, S. Laurent and T. Sen, *Adv. Drug Delivery Rev.*, 2011, **63**, 24–46.
26 M. Mahmoudi, I. Lynch, M. R. Ejtehadi, M. P. Monopoli, F. B. Bombelli and S. Laurent, *Chem. Rev.*, 2011, **111**, 5610–5637.
27 N. Singh, G. J. S. Jenkins, R. Asadi and S. H. Doak, *Nano Rev.*, 2010, **1**, 5358.
28 S. Li, J. Wei, Q. Yao, X. Song, J. Xie and H. Yang, *Chem. Soc. Rev.*, 2023, **52**, 1672–1696.
29 E. B. Ehlerding, F. Chen and W. Cai, *Adv. Sci.*, 2016, **3**, 1500223.
30 Y. Zheng, L. Lai, W. Liu, H. Jiang and X. Wang, *Adv. Colloid Interface Sci.*, 2017, **242**, 1–16.
31 S. Das, S. Tripathy, B. Sreedhar, S. Mukherjee and C. R. Patra, *Adv. Ther.*, 2023, **6**, 2200293.
32 J. Li, J.-J. Zhu and K. Xu, *TrAC, Trends Anal. Chem.*, 2014, **58**, 90–98.
33 J. Sobhanan, J. V. Rival, A. Anas, E. Sidharth Shibu, Y. Takano and V. Biju, *Adv. Drug Delivery Rev.*, 2023, **197**, 114830.
34 X. Wu, X. He, K. Wang, C. Xie, B. Zhou and Z. Qing, *Nanoscale*, 2010, **2**, 2244.
35 C. Zhang, Z. Zhou, Q. Qian, G. Gao, C. Li, L. Feng, Q. Wang and D. Cui, *J. Mater. Chem. B*, 2013, **1**, 5045.
36 M. Mahmoudi, M. P. Landry, A. Moore and R. Coreas, *Nat. Rev. Mater.*, 2023, **8**, 422–438.
37 C.-E. Ha and N. V. Bhagavan, *Biochim. Biophys. Acta, Gen. Subj.*, 2013, **1830**, 5486–5493.
38 J. S. Mohanty, P. L. Xavier, K. Chaudhari, M. S. Bootharaju, N. Goswami, S. K. Pal and T. Pradeep, *Nanoscale*, 2012, **4**, 4255.
39 X. Dou, X. Yuan, Y. Yu, Z. Luo, Q. Yao, D. T. Leong and J. Xie, *Nanoscale*, 2014, **6**, 157–161.
40 J.-P. Jolivet, C. Chanéac and E. Tronc, *Chem. Commun.*, 2004, 477–483.
41 R. Ostruszka, D. Půlpánová, T. Pluháček, O. Tomanec, P. Novák, D. Jirák and K. Šišková, *Nanomaterials*, 2023, **13**, 1027.
42 S. Shankar, N. S. K. Gowthaman, P. Arul, F. Chen, H. N. Lim and F.-X. Qin, *New J. Chem.*, 2021, **45**, 1278–1285.
43 N. Tyagi, P. Gupta, Z. Khan, Y. R. Neupane, B. Mangla, N. Mehra, T. Ralli, A. Alhalmi, A. Ali, O. Al Kamaly, A. Saleh, F. A. Nasr and K. Kohli, *Molecules*, 2023, **28**, 2343.
44 L. Gonzalez-Moragas, S.-M. Yu, E. Carenza, A. Laromaine and A. Roig, *ACS Biomater. Sci. Eng.*, 2015, **1**, 1129–1138.
45 R. Ostruszka, G. Zoppellaro, O. Tomanec, D. Pinkas, V. Filimonenko and K. Šišková, *Nanomaterials*, 2022, **12**, 1425.
46 T. Geng, L. Zhao, D. Wu, H. Zhang, X. Zhao, M. Jiao and L. Zeng, *ACS Appl. Nano Mater.*, 2021, **4**, 13818–13825.
47 A. Mathew, P. R. Sajanlal and T. Pradeep, *J. Mater. Chem.*, 2011, **21**, 11205.
48 X.-D. Zhang, D. Wu, X. Shen, P.-X. Liu, F.-Y. Fan and S.-J. Fan, *Biomaterials*, 2012, **33**, 4628–4638.
49 I. Nandi, S. Chall, S. Chowdhury, T. Mitra, S. S. Roy and K. Chattopadhyay, *ACS Omega*, 2018, **3**, 7703–7714.
50 P. Khullar, V. Singh, A. Mahal, P. N. Dave, S. Thakur, G. Kaur, J. Singh, S. Singh Kamboj and M. Singh Bakshi, *J. Phys. Chem. C*, 2012, **116**, 8834–8843.
51 P. Goegan, G. Johnson and R. Vincent, *Toxicol. In Vitro*, 1995, **9**, 257–266.
52 Y. Feng, G. Wang, Y. Chang, Y. Cheng, B. Sun, L. Wang, C. Chen and H. Zhang, *Nano Lett.*, 2019, **19**, 4478–4489.
53 F. Chen, P. Huang, Y.-J. Zhu, J. Wu, C.-L. Zhang and D.-X. Cui, *Biomaterials*, 2011, **32**, 9031–9039.
54 P. Zhang, X. X. Yang, Y. Wang, N. W. Zhao, Z. H. Xiong and C. Z. Huang, *Nanoscale*, 2014, **6**, 2261–2269.
55 A. Zhang, Y. Tu, S. Qin, Y. Li, J. Zhou, N. Chen, Q. Lu and B. Zhang, *J. Colloid Interface Sci.*, 2012, **372**, 239–244.
56 L. Chen, Y. Zhang, H. Jiang, X. Wang and C. Liu, *Chin. J. Chem.*, 2016, **34**, 589–593.
57 Z. Zhou, L. Yang, J. Gao and X. Chen, *Adv. Mater.*, 2019, **31**, 1804567.
58 M. Rohrer, H. Bauer, J. Mintorovitch, M. Requardt and H.-J. Weinmann, *Invest. Radiol.*, 2005, **40**, 715–724.

59 K. Rurack and M. Spieles, *Anal. Chem.*, 2011, **83**, 1232–1242.
60 D.-E. Lee, H. Koo, I.-C. Sun, J. H. Ryu, K. Kim and I. C. Kwon, *Chem. Soc. Rev.*, 2012, **41**, 2656–2672.
61 S.-K. Sun, L.-X. Dong, Y. Cao, H.-R. Sun and X.-P. Yan, *Anal. Chem.*, 2013, **85**, 8436–8441.
62 D.-H. Hu, Z.-H. Sheng, P.-F. Zhang, D.-Z. Yang, S.-H. Liu, P. Gong, D.-Y. Gao, S.-T. Fang, Y.-F. Ma and L.-T. Cai, *Nanoscale*, 2013, **5**, 1624.
63 C. Unruh, N. Van Bavel, M. Anikovskiy and E. J. Prenner, *Molecules*, 2020, **25**, 5762.